Mechatronics 56 (2018) 198–210

Contents lists available at ScienceDirect

Mechatronics

journal homepage: www.elsevier.com/locate/mechatronics

An adjustable-stiffness MEMS force sensor: Design, characterization, and control☆

Mohammad Maroufi*, Hamed Alemansour, M. Bulut Coskun, S. O. Reza Moheimani*

Department of Mechanical Engineering, University of Texas at Dallas, Richardson, TX 75080, USA

ARTICLE INFO

Keywords:
Microelectromechanical Systems (MEMS)
Force Sensor
Stiffness Adjustment Mechanism
Piezoresistive Sensor
Resonant Controller
Internal Model Controller

ABSTRACT

This paper presents a novel one-degree-of-freedom microelectromechanical systems (MEMS) force sensor. The high-bandwidth device contains on-chip sensing and actuation mechanisms, enabling open- and closed-loop modalities. An active compliance mechanism is incorporated to render the device more conducive to characterization of soft samples. When operated in closed loop, the adjustable stiffness enables the sensor to attain a larger dynamic range and minimize the nonlinearities originating from flexures. Analytical models are employed to design and calibrate the sensor. In open loop, the sensing resolution of 23.3 nN within a bandwidth of 2.35 kHz and a full-scale range of $\pm$ 42.6 µN are experimentally obtained. The resolution is enhanced to 9.3 nN by employing an active compliance mechanism. When operated in closed loop, a resolution of 12.9 nN is achieved within a dynamic range of 71.2 dB and a sensing bandwidth of 3.6 kHz is demonstrated. The sensor performance is tested by obtaining the stiffness of an atomic force microscope probe and measuring the force produced by a self-actuated piezoelectric microcantilever.

1. Introduction

Force sensors play a pivotal role in a myriad of applications in science and technology. Development of high-precision force sensors can lead to the development of novel methods for characterization of various samples and devices, with the potential to making a lasting impact on a number of disciplines.

A powerful tool for measuring force in the range of pico- to nanonewtons is atomic force microscope (AFM) probe [1]. Measuring stiffness of different types of cells and determining binding properties of biomolecules [2] are among successful examples of employing these force sensors.

AFM probes are fabricated using processes developed for microelectromechanical systems (MEMS). Highly-sensitive force sensors are also realized by exploiting MEMS technology, which feature mechanical flexures, on-chip displacement sensors, and in some cases on-chip actuators [3,4]. These force sensors can be implemented either as standalone devices or integrated within other systems. Micro-grippers are a prominent example of the latter which are used for manipulation and characterization of small objects [5–7]. Due to the flexibility in the design of MEMS force sensors, a wide spectrum of measurement ranges, degrees of freedom, and resolutions can be achieved, offering more versatility compared to AFM cantilevers. Thus, sensing properties offered by MEMS force sensors can potentially fill the existing gap between AFM-based methods and macro-scale conventional sensors. Although, it should be pointed out that MEMS force sensors whose measurement precision surpasses those of typical AFM probes have been reported in the literature, e.g. the sensor with femtonewton resolution in [8].

Characterization of micron-sized samples is perhaps the main objective for developing MEMS force sensors. In [9], a dual-axis MEMS force sensor with a range of 110 µN and a resolution of 33.2 nN along each axis is proposed for characterization of soft hydrogel microparticles. A MEMS device featuring both displacement and force sensing is proposed in [10]. Stiffness measurement of AFM microcantilevers is addressed by proposing a MEMS force sensor in [3,4]. In [11], a MEMS force sensing array is used to characterize dynamics of cell membranes. Measuring heart cell force[12], and obtaining mechanical properties of mouse zona pellucida in [13] are also the other examples of these applications.

In characterization of delicate samples, the relative stiffness of MEMS force sensor and samples plays a crucial role. Using a stiff force sensor can inflict a large deflection/deformation on the sample before the interaction force becomes measurable. This may reduce the

☆ This paper was recommended for publication by Guest Editor Dr. Jason Gorman.

* Corresponding authors.
E-mail addresses: mohammad.maroufi@utdallas.edu (M. Maroufi), hamed.alemansour@utdallas.edu (H. Alemansour), bulut.coskun@utdallas.edu (M. Bulut Coskun), reza.moheimani@utdallas.edu (S. O. Reza Moheimani).

https://doi.org/10.1016/j.mechatronics.2018.05.007
Received 26 July 2017; Received in revised form 15 March 2018; Accepted 15 May 2018
Available online 09 July 2018
0957-4158/

measurement accuracy and increase the chance of damaging the sample. Developing a force sensor much more compliant than the sample may be a solution. However, several trade-offs impose limitations on such a design, as the force sensor stiffness has a direct impact on its sensing properties including dynamic range and resolution.

Mechanical flexures in a compliant MEMS force sensor can endure a relatively large deflection within a given external force range. However, for large deflections they are known to behave nonlinearly [14–16], ultimately degrading the force sensor linearity [4]. In [17], this issue is addressed by implementing numerous mechanical frames in a MEMS force sensor, leading to a full-scale range of 1 μ N and a dynamic range of 86 dB. This approach, however, requires a complex mechanical flexure with a large on-chip footprint. More importantly, a large mechanical structure and a displacement of hundreds of micrometers make the implementation of an on-chip sensing mechanism problematic. The displacement measurement in [17] is performed using an optical system and a separate fixed beam as a reference structure, which restricts the portability and versatility of the resulting sensor. Performing force measurement in closed loop, is an alternative approach to mitigate flexural nonlinearity. This method was successfully implemented in [3] to measure stiffness of AFM probes. There, a feedback controller is implemented to maintain the null position of the mechanical flexure by applying a balancing force using an embedded actuator, and the control signal is then used as a measure of the applied force. Closed-loop operation mitigates the nonlinearity, and to some extent decouples the sensor sensitivity from full-scale range of the device [18]. Even though the closed-loop operation can lead to a linear force sensor, the problem of measuring the stiffness of soft samples still remains in [3] as the sensor's mechanical stiffness is relatively large compared to the soft AFM probes.

To address the compliance mismatch, a force sensor featuring an on-chip stiffness-adjusting mechanism is presented in this work. Similar mechanisms were previously reported by others; for a review see [19]. By *in-situ* changing the system's stiffness, this mechanism essentially provides a "knob" to tune the force sensor characteristics according to each sample's properties. On-chip actuation and sensing mechanisms are also incorporated to make the device portable and ready for control implementation. While the novel concepts presented within this device can be employed for implementing future MEMS force sensors, measuring the stiffness of AFM probes is the particular application that was kept in mind during the design. In this work, by employing AFM probes, the performance of the proposed MEMS force sensor is investigated.

The remainder of the paper continues as follows. In the next section, force sensing concepts are briefly explained. Design and fabrication of the MEMS sensor are detailed in Section 3. Characterization of the device is presented in Section 4. In Section 5, controller design and implementation are reported. Performance of the force sensor in open and closed loop are explored in Section 6. The results are further discussed and compared with prior works in Section 7, and the paper is concluded in Section 8.

2. Force sensing concept

The static-mode force sensing can be performed in open or closed loop.[1] Fig. 1a illustrates the concept of open-loop force sensing. Here, the mechanical stiffness of the force sensor (k) is known, and the probe displacement (x) induced by an external force (F_{ext}) is measured using a displacement sensor. The external force can then be obtained by using Hook's law as $F_{ext} = kx$. In this case, the resolution of the force sensor is directly proportional to that of the displacement sensor. In addition, the mechanical stiffness directly affects the force sensor resolution, bandwidth, and its full-scale range, while k being constant throughout the probe displacement range plays a pivotal role in sensor's linearity.

As shown in Fig. 1b, for operations in closed loop, the displacement sensor measures the initial displacement of the probe induced by the external force. Then, the controller generates a command signal (u) to move the actuator so as to nullifying the effect of the external force. Therefore, the command signal (u) is proportional to the external force i.e. $F_{ext} = \alpha u$, where α is a function of the actuator's properties. Here, the force sensing resolution is determined in terms of the noise content of u. Other characteristics such as sensor linearity and full-scale range depend on the embedded actuator properties. Note that, on the contrary to the open-loop modality, the resolution and full-scale range of the force sensor can be independently tuned in closed loop.

In both open- and closed-loop modalities, mechanical stiffness of force sensors significantly affects their properties. In particular, if a sensor is designed for characterization of soft samples, its mechanical stiffness turns out to have a more pronounced effect. Fig. 1c is a schematic demonstration of a test set-up where a force sensor interacts with a samples with a much smaller stiffness (i.e. $k_s \ll k$). Here, an external positioner is used to push the force sensor toward the sample. The smallest measurable displacement (x_{min}), and the corresponding sample deformation (x_s) are related according to:

$$x_s = \frac{kx_{min}}{k_s} \tag{1}$$

Now, (1) implies that to reach a measurable displacement, the sample should undergo a large deflection since $k/k_s \gg 1$. To address this issue, either the resolution of the displacement sensor should be improved or the stiffness of the sensor (k) should be reduced. In this work, we use a displacement sensor with nanometer-range resolution and implement a stiffness-adjusting mechanism.

3. Design and fabrication

The structure of the proposed force sensor is schematically shown in Fig. 2. The device comprises a probe at the center featuring a sharp tip at one end to interact with samples. Clamped-guided flexures are implemented to serve as suspensions. In order to measure the probe bidirectional rectilinear displacement, a tilted-beam bulk piezoresistive sensor is incorporated [22]. For actuation, an on-chip electrostatic comb-drive structure is used [14]. The stiffness-adjustment mechanism is the other crucial part of the device realized using parallel-plate capacitive structures for *in-situ* tuning of the sensor characteristics. The design of the device components are further detailed next.

3.1. Piezoresisitve displacement sensor

Having an on-chip displacement sensing mechanism can render the force sensor portable and thus adaptable for numerous measurement applications. As explained in Section 2, a large dynamic range as well as fine resolution offered by the embedded displacement sensor can also translate directly to the same specifications in the force sensor.

Various on-chip sensing mechanisms, e.g. capacitive [23], electrothermal [24], and piezoresistive [25], can be exploited to fulfill such requirements. Capacitive sensing typically renders a nanometer-range resolution with a relatively large bandwidth. However, this mechanism is prone to parasitic capacitance and may require a complex readout circuitry. In addition, in order to realize on-chip sensing capacitors, a large on-chip structure may be needed which in turn increases the size and reduces the device's mechanical bandwidth.

Electrothermal displacement sensors provide a resolution also in nanometer range with a less-complex circuitry, while featuring a small form-factor. However, these sensors typically suffer from a limited bandwidth [26].

In [22,27], we proposed a bulk piezoresistive displacement sensor with nanometer measurement resolution. This sensor does not require a complex readout circuit, and may serve as a mechanical flexure of the

[1] The dynamic-mode force sensing (such as in [20,21]) is beyond the scope of this paper.

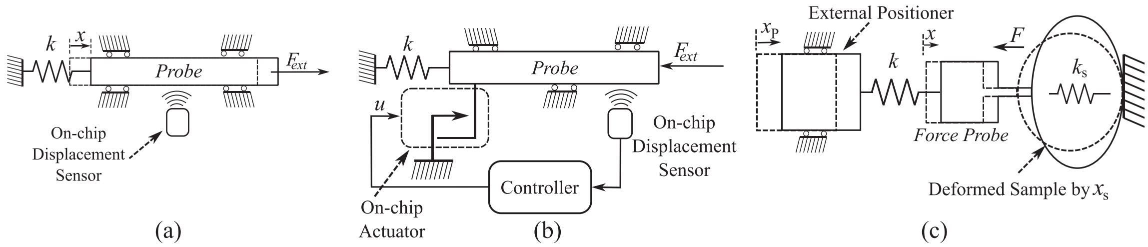

Fig. 1. (a) open-loop and (b) closed-loop sensing modalities. The sensor stiffness is designated by k and symbolically shown by a spring. (c) schematically shows a soft sample interacting with the force probe. Here, $x_p = x + x_s$, and the force (F) is the interaction force between the sample and the force sensor.

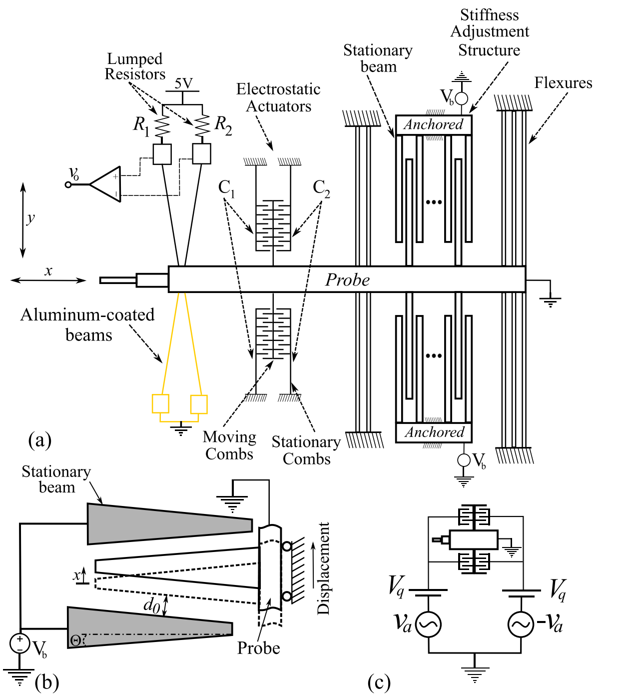

Fig. 2. (a) Schematic of the force sensor, including the readout circuit for the bulk piezoresistive displacement sensor. (b) A moving beam in the stiffness-adjustment structure as the probe moves by x. (c) Schematic of the actuation circuit. The moving beams in (b) and the moving comb fingers in (c) are electrically grounded via the probe.

device reducing the sensor's footprint to be practically zero. For realization, only standard microfabrication process is required with no need for extra masking and doping. This compares positively with conventional piezoresistive displacement sensors where the selective implementation of highly-doped regions is a must. On the contrary to the electrothermal sensors, bulk piezoresistive sensors also demonstrates a superior sensing bandwidth, much smaller drift, and more linearity [28]. These advantages motivated us to use the bulk piezoresistive method within the proposed force sensor.

The structure of the bulk piezoresistive sensor is schematically shown in Fig. 2a. The sensor consists of two pairs of slanted beams in a V-shaped configuration. One pair is used for sensing, while the other is coated with aluminum and electrically grounded. Since prior to the fabrication, the entire top surface of the silicon is heavily doped [29], the bulk piezoresistivity of the sensing beams is used for displacement measurement [22]. As the probe moves, electrical resistances of the sensing beams oppositely change due to their piezoresistivity and the generation of axial forces, which is compressive in one and tensile along the other [22]. An external Wheatstone bridge in a half-bridge configuration then converts the resistance change to a voltage which is further amplified using a differential amplifier.

3.2. Flexures

Mechanical stiffness of the force sensor is due to the combined effects of clamped-guided flexures and the bulk piezoresistive sensor. Referring to Fig. 2, the total mechanical stiffnesses along the x and y axes are designated by K_x, and K_y, respectively. The force sensor characteristics depend on K_x, while K_y is required to protect the comb-drive actuators against snapping-in [14,30]. The stiffnesses of clamped-guided beams as well as bulk piezoresistive sensors are analytically investigated in [14] and [22], respectively.

A finite element model (FEM) of the device is constructed in CoventorWare software. Using FEM and analytical models, the flexures are designed to ultimately tune the stiffness, mode shapes, and resonant frequencies of the device. The structural parameters are reported in Table 1, and the stiffness of $K_x = 25.17$ N/m is obtained for the force sensor using FEM. With characterization of AFM probes being the primary application, stiffness of the force sensor is designed to be comparable to that of commercially-available tapping-mode AFM cantilevers. The first in-plane resonance frequency of the device is obtained at 5.6 kHz, while its out-of-plane modes occur at higher frequencies. This enables the force sensor to be used in potential sensing applications where a high-bandwidth is required.

3.3. Stiffness-adjustment mechanism

The stiffness-adjustment unit is designed using a parallel-plate capacitive configuration. To reduce the added mass of the structure, and consequently increase the achievable bandwidth, trapezoidal-shaped beams are chosen [31]. The moving beams are connected to the probe and are interlaced with the stationary beams. In Fig. 2b, one moving beam is schematically shown. The overlapped length of the beams is designated by L, while the probe undergoes a displacement of x in one direction. The initial air gap between the beams at the null position of the probe is denoted by d_0. Ignoring fringing fields and assuming a thickness of t, the total capacitance between the moving and stationary beams is:

$$C = \frac{2n\epsilon_0 Lt}{d}. \tag{2}$$

Here, n is the number of moving beams, ϵ_0 is the vacuum permittivity, and d denotes the air gap distance. Considering the geometry of the beams in Fig. 2b, we may write $d = d_0 \pm x\cos(\theta)$. By applying V_b to the stationary beams, magnitude of the attraction force between each stationary and moving beams along x axis is:

Table 1
The dimensional properties of the force sensor.

Stiffness	$L \simeq 705$ µm, $n = 18$, $d_0 = 10.5$ µm, $\theta = 1.19°$	
Adj. structure	Trapezoidal: Length: 725 µm, Bases: 60 µm, 30 µm	
Electrostatic Actuators	Air gap: $g = 2$ µm	Engagement: 3 µm
	Trapezoidal: Length: 510 µm, Bases: 20 µm, 48.5 µm	
Clamped-guided Flexures	Length: 862 µm	Width: 4.5 µm
	Length: 450 µm	Width: 3 µm

$$|F| = \left|\frac{\partial U}{\partial x}\right| = \frac{\cos(\theta)}{2}\left|\frac{\partial C}{\partial d}\right| V_b^2. \tag{3}$$

The electrostatic forces acting on each moving beam are in opposite directions. In addition, since the stiffness-adjustment unit is symmetrically designed, these forces are equal in magnitude as long as the moving beams are positioned at the center of the air gap. However, as the probe moves by x, the net force on these beams is no longer zero and can be stated as:

$$F_{net} = Z\cos(\theta)\left(\frac{1}{[d_0 - x\cos(\theta)]^2} - \frac{1}{[d_0 + x\cos(\theta)]^2}\right)V_b^2 \tag{4}$$

where $Z = n\varepsilon_0 Lt$. As shown in (4), the net electrostatic force is displacement dependent and always acts to repel the moving beams further away from their center position. This results in a negative mechanical stiffness (K_n=-$\frac{\partial F_{net}}{\partial x}$) that can be described as:

$$K_n = -Z\cos(\theta)\left[\frac{4d_0\cos(\theta)}{A^2} + \frac{16d_0x^2\cos^3(\theta)}{A^3}\right]V_b^2. \tag{5}$$

where

$$A = d_0^2 - x^2\cos^2(\theta). \tag{6}$$

For a small displacement range, i.e. $x \ll d_0$, (5) is simplified as:

$$K_n = -\frac{4Z\cos^2(\theta)}{d_0^3}V_b^2. \tag{7}$$

Here, K_n is independent of the probe displacement (x) and is only a function of V_b. This implies that a reversible and controllable stiffness variation can be achieved in the force sensor by using V_b.

This analytical model is employed to determine various structural parameters of the stiffness-adjusting mechanism. The design objective is to achieve a wide stiffness manipulation range compared to the device's initial stiffness. By employing FEM together with this analytical model, we were able to explore how various parameters affected mode-shapes and resonant frequencies of the device.

Using the tuned parameters in Table 1, properties of the stiffness-adjusting mechanism are further explored in Fig. 3. The absolute value of K_n, obtained from (5), is presented in Fig. 3a as a function of the probe displacement for various V_b. As is clear, the magnitude of the negative stiffness increases nonlinearly with the probe displacement, while the deviation from the linear remains below 10% for displacements up to $\pm$ 1.4 µm at all adjusting voltages. Moreover, the stiffness can be tuned in a wide range by varying V_b compared to its initial calculated value of 25.17 N/m.

Using the analytical model, the external force (F_{ext}) required to induce a linearly increasing displacement in the probe is also calculated. For the probe displacement we have:

$$x = \frac{F_{ext}}{[K_x - |K_n(x)|]} \tag{8}$$

where, $K_x = 25.17$ N/m is the stiffness at $V_b = 0$ V. In Fig. 3b, the probe displacement is shown as a function of the exerted force, where a linear behavior is observable at $V_b = 0$ V as expected. However, by increasing V_b, the linear region shrinks. Here, a turning point can be identified for adjusting voltages above 40 V, (i.e. $V_b \geq 40$ V), beyond which larger displacements can be only obtained by reducing the force. This point identified as "A" in Fig. 3b for $V_b = 60$ V. Exerting a larger force beyond this point leads to uncontrolled large displacements of the probe, causing it to ultimately hit the on-chip mechanical stopper. This was experimentally observed during sensor characterization (Section 4.1). Regarding the result presented in Fig. 3b, the displacement range of $\pm 2\,\mu m$ and the stiffness-adjusting voltages up to 60 V are considered for the device. Importantly, beyond $V_b = 70$ V, the use of the force sensor becomes impractical as its displacement range becomes significantly restricted.

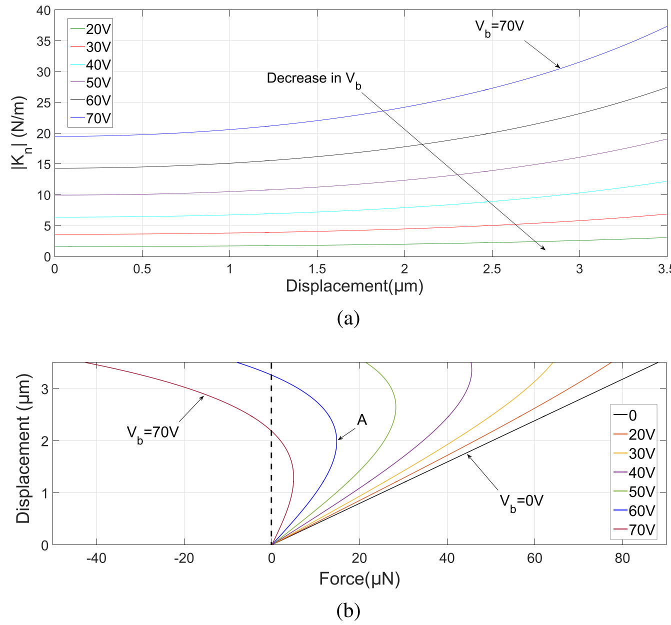

Fig. 3. (a) shows the change in the absolute value of the negative stiffness with respect to the probe displacement at various stiffness-adjusting voltages. (b) The probe displacement versus exerted force at various stiffness adjusting voltages, assuming the initial stiffness to be 25.17 N/m.

3.4. Electrostatic actuators

Electrostatic and electrothermal actuators are widely used in MEMS [14]. In this design, electrostatic actuators are selected over electro-thermal due to their high-bandwidth and low-temperature properties, as well as their low-power requirements.

A schematic of the actuation circuit is depicted in Fig. 2c. The force produced by the electrostatic actuator on each side with the capacitance of C and the actuation voltage of V is:

$$F_{act} = -\frac{\partial U}{\partial x} = -\frac{1}{2}\frac{\partial C}{\partial x}V^2. \tag{9}$$

Here, differential actuation voltages (i.e. $\pm\ v_a$) plus a bias voltage (V_q) are applied to the stationary combs and the moving combs are electrically grounded. As shown in Fig. 2a, the capacitance between moving and stationary combs on opposite sides are identified by C_1 and C_2. Each capacitance is a function of the number of moving comb fingers, the air gap distance between the fingers, and the vacuum permittivity [14]. The force exerted by the stationary combs to the moving ones are in opposite directions. Hence, using (9), the net actuation force on the moving combs is:

$$F_{act} = \frac{1}{2}\left[\left|\frac{\partial C_1}{\partial x}\right|(V_q + v_a)^2 - \left|\frac{\partial C_2}{\partial x}\right|(V_q - v_a)^2\right]. \tag{10}$$

Let us define the comb drive coefficients as $k_{c1} = |\frac{\partial C_1}{\partial x}|$ and $k_{c2} = |\frac{\partial C_2}{\partial x}|$, and thus (10) is rewritten as:

$$F_{act} = \frac{(k_{c1} - k_{c2})}{2}v_a^2 + (k_{c1} + k_{c2})V_q v_a + \frac{(k_{c1} - k_{c2})V_q^2}{2} \tag{11}$$

which is a nonlinear function of the actuation voltage (v_a). However, since the actuators are symmetrically designed, we have $k_{c1} = k_{c2} = k_c$ provided that the fabrication tolerances remain negligible. In this case, F_{act} is simplified to

$$F_{act} = 2k_c V_q v_a \tag{12}$$

indicating that the net actuation force will be a linear function of v_a in an accurately-fabricated device. The comb-drive coefficients ($k_{c1,\ 2}$) are experimentally obtained in Section 4.2, and the linearity of the

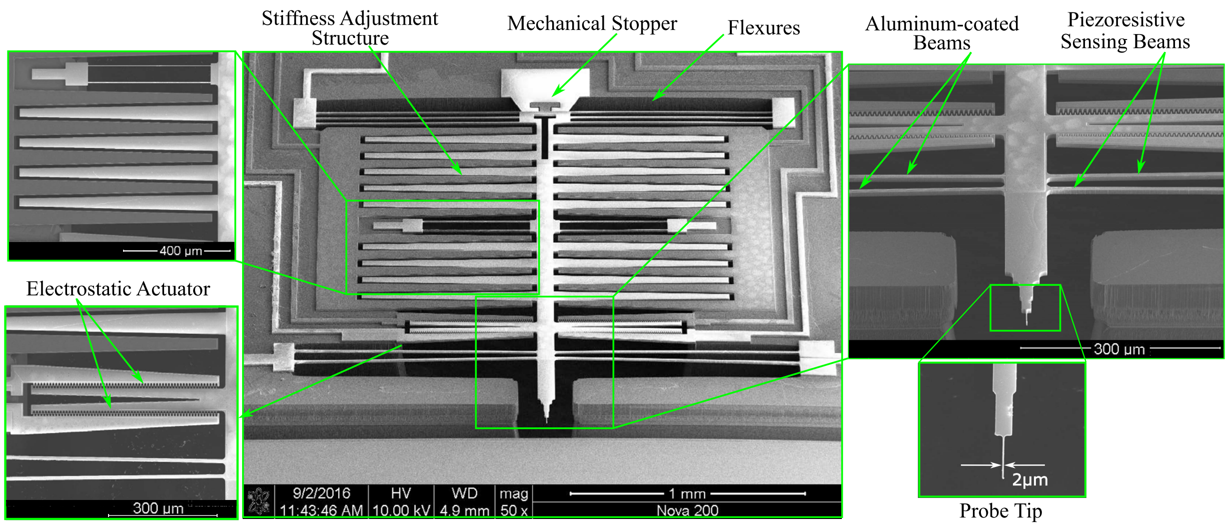

Fig. 4. SEM image of the force probe. The electrostatic actuators, piezoresistive displacement sensor, stiffnesses adjustment structure, and the probe tip are shown in close-up views. The thickness of the device is 10 μm.

actuation force is also discussed.

The linearity obtained using this actuation mechanism can drastically mitigate the well-known quadratic behavior of the comb-drive electrostatic actuators [14]. Compared to the nonlinear electrostatic actuation employed in the MEMS force sensor reported in [3], this actuation mechanism can reduce the complexity of the control system.

3.5. Fabrication

The scanning electron microscope (SEM) image of the force sensor is shown in Fig. 4. The device is fabricated using MEMSCAP's PiezoMUMPs standard microfabrication process [29]. The dimensional limitations imposed by this fabrication process are also considered during the design. The fabrication is performed using a silicon-on-insulator (SOI) wafer with a 10 µm-thick device layer doped on the top surface. Note that, we did not use the available piezoelectric layer for the realization of this device.

4. Characterization

4.1. Mechanical characterization

In-plane displacement of the probe is measured in time domain using a Polytec Micro System Analyzer (MSA-100-3D). During the test, the actuation is performed using the circuit schematically shown in Fig. 2c while V_q is set to 45 V. In Fig. 5, the probe displacement is presented as a function of the actuation voltage (v_a). To examine the effect of stiffness-adjustment voltages (V_b), the experiments are performed while this voltage is varied within the range of 0 V to 60 V. As evident in Fig. 5, the probe undergoes a larger displacement for a given actuation voltage by increasing V_b indicating a decrease in the device's stiffness. Based on the analytical model presented in Section 3.3, the limited displacement range observable at V_b = 60 V is anticipated (point A in Fig. 3b).

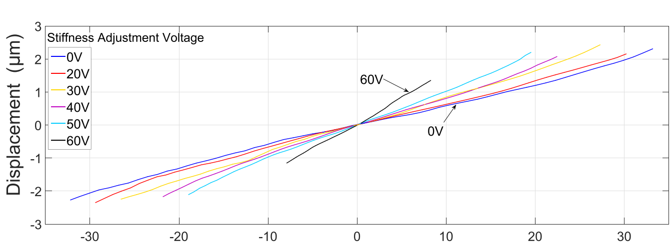

Fig. 5. Displacement of the probe versus actuation voltage (v_a) at different stiffness-adjustment voltages ranging from 0 V to 60 V.

During the experiments, the output of the piezoresistive displacement sensor is simultaneously recorded. A linear mapping is observed between the piezoresistive sensor output and the probe displacement. Using the recorded data and the measured displacement, piezoresistive sensor's calibration factor is calculated as − 0.107 V/μm. The same calibration factor is obtained for various stiffness-adjustment voltage (V_b), as expected.

Frequency response of the device from the actuation signal to the output of the piezoresistive sensor is also obtained over a frequency range of 10 kHz and is presented Fig. 6 for varying V_b values. As shown, the resonant frequency shifts from 4.48 kHz for V_b = 0 V to 2.88 kHz for V_b = 60 V. Correspondingly, the sensor stiffness decreases about 2.41 times from its original value, which is also observable as a rise of 7.6 dB in the dc-gain. These results show that an increase in V_b renders the device more compliant, indicating that the in-plane dynamics of the device can be manipulated using the stiffness-adjustment mechanism.

4.2. Comb-drive coefficients and sensor stiffness

From (11), we note that the actuation force is a function of the comb-drive coefficients (i.e. $k_{c1,\ 2}$). Knowing these parameters enables us to determine the force generated by the actuators, and consequently, to calibrate the force sensor. These parameters plus the sensor stiffness are three unknowns which are simultaneously determined through experiments described next.

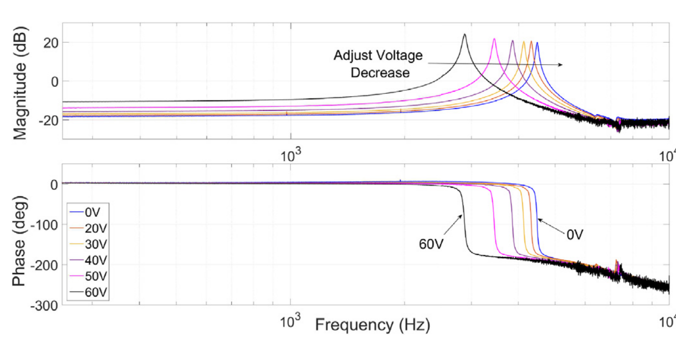

Fig. 6. Frequency response of the force sensor from its embedded actuation input to the output of piezoresistive displacement sensor at various stiffness-adjustment voltages.

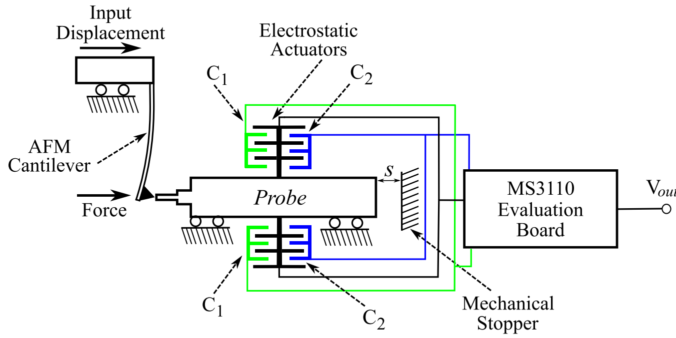

Fig. 7. The test set-up implemented to measure the comb-drive coefficients of the electrostatic actuators. The force sensor's probe is pushed by a cantilever to the right to close the air gap (s). The output voltage of the MS3110 evaluation board is proportional to the capacitance change of the electrostatic actuators (i.e. $V_{out}\,[C_1 - C_2]$).

The setup for the first experiment is schematically shown in Fig. 7. During the test, the probe is externally pushed until it comes into contact with the mechanical stopper. This is done using an external positioner and a high-stiffness AFM cantilever (Bruker RTESP-525). Since the distance between the probe and the mechanical stopper (s in Fig. 7) is fabricated to be 3.5 μm, the displacement of the probe is known within the fabrication tolerances. Simultaneously, the differential variation in the comb fingers capacitance (i.e. $[C_1 - C_2]$) is measured to be 88.4 fF using an Irvine Sensors MS3110 evaluation board. Using the definition of $k_{c1,\,2}$ while the displacement (3.5 μ m) and the resulting capacitance change (88.4 fF) are being known, we have:

$$k_{c1} + k_{c2} = 2.562 \times 10^{-8}\ F/m. \tag{13}$$

In a second experiment, the last term in the right-hand-side of (11) is obtained by applying only the dc-bias voltage to the actuators (i.e. $V_q = 45$ V, $V_b = v_a = 0$ V) and recording the displacement sensor output. Due to the symmetry, we expected that $k_{c1} = k_{c2}$, and therefore, zero actuation force and probe displacement occur in this test. However, a probe displacement of $x_0 = 21.4$ nm is obtained by the piezoresistive sensor, indicating a mismatch between the actuators on each side, most likely due to fabrication tolerances. With K_x denoting the unknown stiffness of the force sensor at $V_b = 0$ V, Hook's law can be written using (11) as:

$$\frac{(k_{c1} - k_{c2})V_q^2}{2} = K_x x_0 \tag{14}$$

and therefore, for comb-drive coefficients we have:

$$k_{c1} - k_{c2} = \frac{2K_x x_0}{V_q^2}. \tag{15}$$

The third equation is obtained by fitting a line on the displacement-actuation data reported in Fig. 5 at $V_b = 0$ V. The fitting is performed within a small displacement range of ± 0.268 μ m, ensuring that the sensor stiffness (K_x) is constant. With p denoting the slope of the fitted line, Hook's law is then written as:

$$F_{act} = K_x p v_a. \tag{16}$$

Here, the actuation voltage of $v_a = 4.85$ V, corresponding to probe displacement of 0.268 μm, is considered. Replacing F_{act} from (11) in (16), and solving (13), (15), and (16) simultaneously, the unknowns are obtained and reported in Table 2. Replacing k_{c1} and k_{c2} in (11), the actuation force is also obtained as a function of v_a as:

$$F_{act} = 2.247 \times 10^{-10} v_a^2 + 1.153 \times 10^{-6} v_a + 4.549 \times 10^{-7}. \tag{17}$$

The quadratic term in the actuation force is four orders of magnitude smaller than the linear term. This induces about 0.8% deviation from linear within the range of 40V for v_a. The difference between the force sensor stiffness ($K_x = 21.28$ N/m) experimentally obtained here and the stiffness obtained by FEM in Section 3.2 is most likely due the microfabrication tolerances.

Table 2
The stiffness and the comb-drive coefficients which are experimentally obtained.

K_x (N/m)	k_{c1} (F/m)	k_{c2} (F/m)
21.28	1.304×10^{-8}	1.259×10^{-8}

4.3. Piezoresistive sensor noise

To quantify sensor's displacement measurement resolution, sensor noise is recorded in time domain with the sampling rate of 25 kHz for 20 s. A low-pass filter (Stanford Research SR650 Low-noise Filter) with a cutoff frequency of 10 kHz and 115 *dB/Octave* roll-off is also incorporated in series with the sensor output. After removing the mean value of the noise data, the 1σ-resolution of the sensor is calculated as the root mean square (RMS) of the noise signal. By converting the noise RMS to displacement using the piezoresistive sensor's calibration factor (reported in Section 4.1), the 1σ-resolution of 1.43 nm is obtained.

5. Controller design and implementation

Prior to controller design, frequency response of the force sensor in Fig. 6 is used to identify its dynamics. A second-order model, $G(s)$, is identified for the system with the resonant frequency ω_n being a function of the stiffness-adjustment voltage (V_b). For the sake of clarity, the dc-gain is set to unity.

$$G(s) = \frac{\omega_n^2}{s^2 + 2\zeta\omega_n s + \omega_n^2} \tag{18}$$

Assuming a mass-spring-damper model, the resonant frequency (ω_n) is expected to be proportional to the square root of the device stiffness. The device stiffness, on the other hand, is shown to be a quadratic function of V_b based on the model presented in Section 3.3. The device resonant frequency is plotted in Fig. 8 as a function of V_b. Eq. (19) is fitted to the experimental data showing the behavior predicted from the analytical model.

$$\omega_n = \sqrt{-3286 V_b^2 + 2.004 \times 10^7} \tag{19}$$

The damping ratio (ζ) is obtained for the system with various V_b using the least squares method in the frequency domain. As is expected, the change of this parameter is negligible with V_b, and thus, the average value of 0.0058 is selected for the force sensor across all stiffness-adjustment voltages. The constant damping ratio plus the negligible error of the fitted curve in Fig. 8 enable us to substitute (19) in (18) to

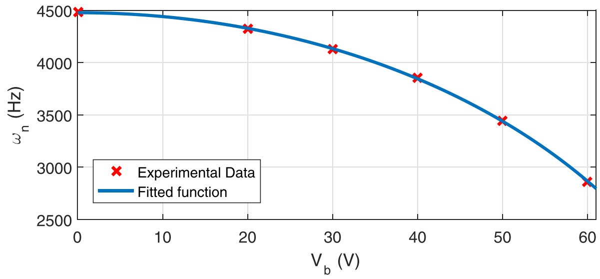

Fig. 8. Variation of the force sensor resonant frequency with respect to the stiffness-adjustment voltage (V_b).

achieve a generalized transfer function valid for all V_b, which adequately models the system dynamics.

In Fig. 9, a schematic of the implemented control loop is shown. The working condition of the force sensor can be closely approximated with this model while the extraneous force is modeled as an input disturbance (w). Here, the control signal (u) is proportional to the extraneous force.

The under-damped nature of the force sensor ($\zeta = 0.0058$) can lead to instability or small stability margins. To alleviate this, a damping controller [$C_1(s)$ in Fig. 9] is designed in an inner feedback loop. A variety of methods such as positive position feedback (PPF) [32], velocity feedback [33], integral resonant controller (IRC) [34] and resonant controller [35], can be used for this purpose. Here, a resonant controller is implemented due to its simple structure and guaranteed closed-loop stability. Since we have obtained a generalized transfer function in (18) for the entire variation range of stiffness-adjustment voltages, a generalized resonant controller is also designed for all V_b as:

$$C_1(s) = \frac{1.2s^2}{s^2 + 140(2\zeta\omega_n)s + 0.81\omega_n^2}. \tag{20}$$

Controller parameters are selected by inspection and the frequency response of the force sensor with the inner loop is obtained for various stiffness-adjustment voltages as shown in Fig. 10. The resonant controller effectively damps the oscillatory dynamics of the force sensor. Here, the resonant peak is attenuated by more than 25 dB for all the three stiffness-adjustment voltages. The same behavior is also observed for other values of $V_b \leq 60$ V. Damping effect of the resonant controller in time domain can also be seen on the step response of the system in Fig. 11. Here, V_b is adjusted to 30 V. A similar response for all values within the permissible range of V_b is observable. The settling time of 5% of the final value is approximately reduced from about 17 ms in the open loop to 1.65 ms in the closed loop for all stiffness-adjustment voltages. The control system can be augmented with additional compensators in an outer feedback loop. Two possibilities are described next.

5.1. Integral controller

The primary control objective of the outer loop [$C_2(s)$] is to keep the probe at its null position. An integral controller presented in (21) is

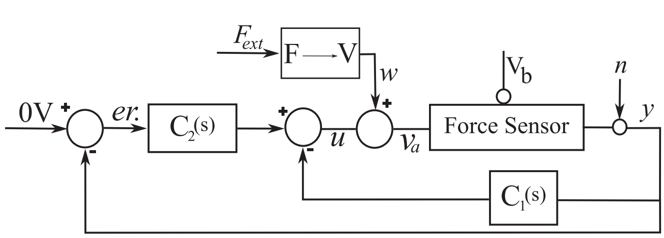

Fig. 9. Block-diagram of the feedback control loop. The input actuation signal to the force sensor is v_a, the external force is modeled as a disturbance (w), (u) is a measure for the extraneous force, and ($er.$) is the tracking error.

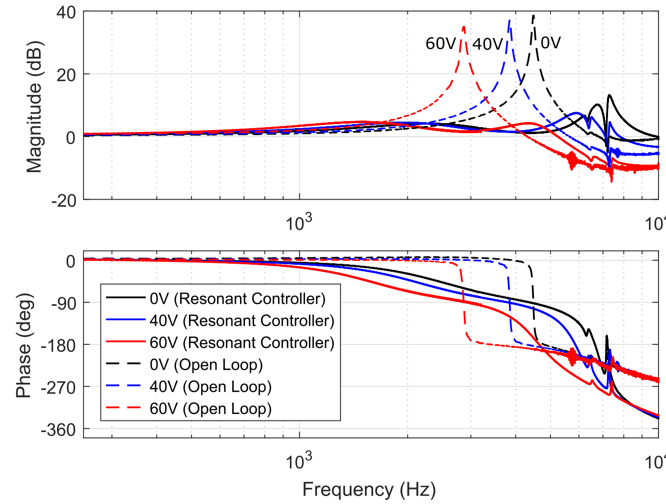

Fig. 10. The frequency response of the force sensor in open loop and closed loop with the resonant controller for V_b = 0 V, 40 V, and 60 V.

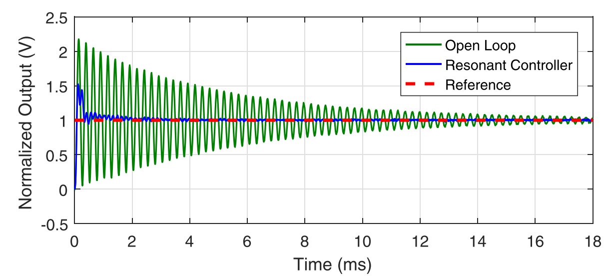

Fig. 11. The step responses of the MEMS force sensor at V_b = 30 V in open loop and with the damping loop. The overshoot and the settling time are significantly improved, while the latter is decreased from 17 ms in open loop to 1.65 ms by using the resonant controller.

initially designed and implemented to track the zero reference signal.

$$C_2(s) = \frac{k_i}{s}. \tag{21}$$

Based on the gain and phase margins of the closed-loop system, the integral gain (k_i) is adjusted to 8000. Phase and gain margins of 35.5° and 5.44 dB, are obtained for V_b = 60 V. Larger margins are achieved for lower values of V_b.

Revisiting the closed-loop model of the force sensor in Fig. 9, performance of the force sensor can be assessed using the transfer function from the input disturbance (w) to the output of the controller (u) as:

$$T_{uw} = \frac{u}{w} = \frac{-G(s)[C_1(s) + C_2(s)]}{1 + G(s)[C_1(s) + C_2(s)]}. \tag{22}$$

T_{uw} is experimentally obtained in the frequency domain and shown in Fig. 12a for several values of V_b. Magnitude of the controller output follows the input force signal over a wide range of frequencies. However, the delay in the phase response starts at much lower frequencies. Force measurement bandwidth defined as the $\pm$ 3 dB point of T_{uw} is about 3.6 kHz for V_b = 60 V. This bandwidth slightly increases at lower stiffness-adjustment voltages. In [36], we reported a relatively large displacement error (designated by $er.$ in Fig. 9) for repetitive disturbance signals (designated by w in Fig. 9) arising from the phase lag of the integrator. To obtain a smaller phase lag, the design of an internal model controller (IMC) is attempted next.

5.2. Internal model control

The second controller which is considered for the $C_2(s)$ is an internal

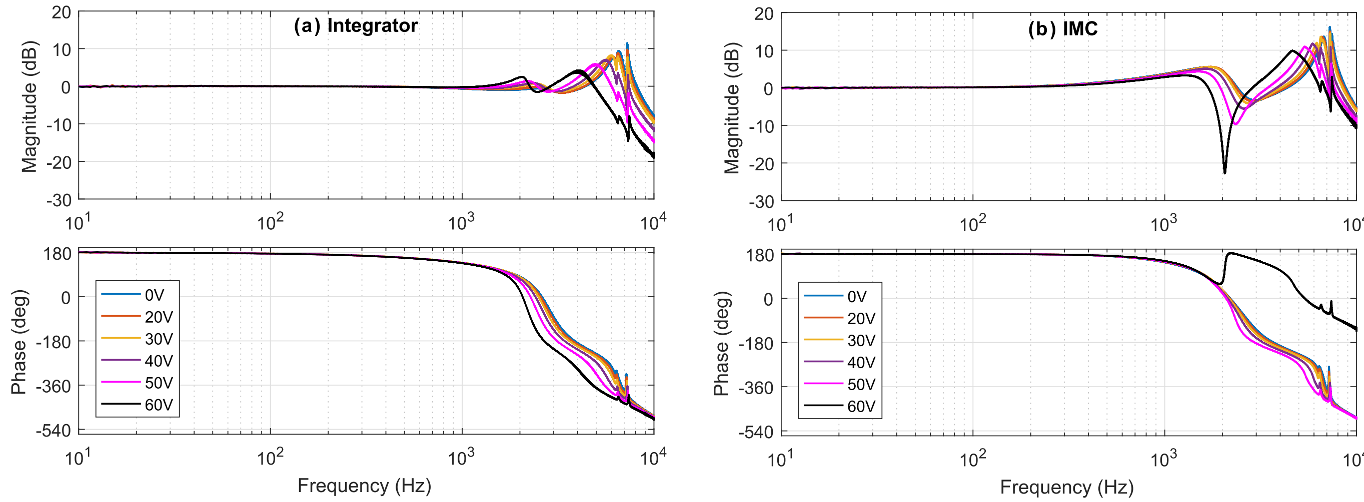

Fig. 12. Closed-loop frequency responses of (a) the integral controller and (b) IMC. The phase lag at e.g. $f = 100$ Hz with the integral controller decreases from 5° to 0.5° after using IMC at the same frequency.

model controller (IMC). This control design method can be employed to compensate for certain classes of deterministic disturbances or to track particular reference signals [37,38]. The plant, for which an IMC is designed, is the damped force sensor described in the beginning of Section 5 with its transfer function expressed as:

$$G(s) = \frac{B(s)}{A(s)} \tag{23}$$

where

$$A(s) = s^4 + 282\zeta\omega_n s^3 \tag{24}$$

$$+ (3.01 + 560\zeta^2)\omega_n^2 s^2 + 281.62\zeta\omega_n^3 s + 0.81\omega_n^4$$

$$B(s) = \omega_n^2(s^2 + 280\zeta\omega_n s + 0.81\omega_n^2). \tag{25}$$

For disturbances in a stable feedback loop, internal model principle states that when the polynomial which generates the disturbance is included in the controller denominator, the disturbance will be asymptotically compensated. Here, the controller structure is as follows:

$$C_2(s) = \frac{A(s)P(s)}{\Gamma(s)L(s)}, \tag{26}$$

where $P(s)$ and $L(s)$ are polynomials to be determined, $\Gamma(s)$ is the disturbance generating polynomial, and $A(s)$ is the plant denominator. Note that, having $A(s)$ in the numerator of $C_2(s)$ helps to reduce the order of the forward transfer function by four. Here, the simplified closed-loop characteristic polynomial is:

$$A_{cl}(s) = \Gamma(s)L(s) + B(s)P(s). \tag{27}$$

Ramp-like exogenous forces occur when the force sensor is steadily pushed against a sample. The effect of this disturbance vanishes asymptotically if the IMC includes two poles at the origin ($\Gamma(s) = s^2$). Note that adding another pole to the integral controller (Section 5.1) is not feasible as it renders the system unstable. Based on the pole placement method, the poles of closed-loop system can be arbitrarily specified as long as the degree of biproper controller is at least five. Hence, the controller is expressed as:

$$C_2(s) = \frac{A(s)(\beta_1 s + \beta_0)}{s^2(s^3 + \alpha_2 s^2 + \alpha_1 s + \alpha_0)}. \tag{28}$$

This leads to the following pole assignment equation:

$$A_{cl}(s) = s^2(s^3 + \alpha_2 s^2 + \alpha_1 s + \alpha_0) + B(s)(\beta_1 s + \beta_0), \tag{29}$$

where $A_{cl}(s)$ is the desired characteristic polynomial of the closed-loop system. Poles of $A_{cl}(s)$ are selected (in kHz) as follows:

$$\{-1.4 \pm 0.75i, -2, -3.5, -5\}. \tag{30}$$

Using (29), the unknown coefficients α_0, α_1, α_2, β_0, β_1 are then evaluated. Selection of these poles results in the desired stability margins, closed loop bandwidth, and transient response of the system.

With this IMC, T_{uw} is experimentally obtained in the frequency domain and shown in Fig. 12b. Compared with the integral controller, phase responses are significantly improved. However, magnitude of the response deviates from 0 dB at lower frequencies for all stiffness adjustment voltages. The minimum force measurement bandwidth is defined as $\pm$ 3 dB point of T_{uw}, approximately 800 Hz at $V_b = 0$V.

In order to evaluate the controller performance, a disturbance voltage (w) is applied to the force sensor to simulate the effect of an external force. The force (F) is converted to a disturbance voltage signal (w) using (17). In this experiment, controller output (u) and probe displacement are simultaneously recorded. Even though the IMC controller is initially designed to track a ramp signal, 100 Hz sinusoidal and triangular signals are chosen in this test to better demonstrate the controller performance. Tracking a triangular setpoint, with sharp turning points, is more demanding than a ramp [39]. Performance of the IMC and integral controllers are compared in Fig. 13. An important observation is that the phase shift at the output and consequently the tracking error are significantly reduced with the IMC, which improves the tracking precision of the force sensor for measuring dynamic forces.

6. Force sensing performance

In order to investigate the force sensor performance in both open and closed loop, an experimental testbed is constructed as described next.

6.1. Experimental setup

The force sensor is glued and wire-bonded to a custom-made printed circuit board (PCB) as shown in Fig. 14. The readout circuit of the piezoresistive sensor is implemented in a separate custom-made PCB (not shown). The experimental test setup is built to physically apply static and dynamic forces to the force sensor. The setup comprises a microfabricated piezoelectric cantilever together with its driving PCB which is attached to a XYZ positioning stage (Newport M-562-XYZ ULTRAlign). The force sensor is mounted on a PCB holder which can be positioned in front of the piezoelectric cantilever using an uni-axial stage (Thorlabs PT1/M). Two microscopes are used to attain the top

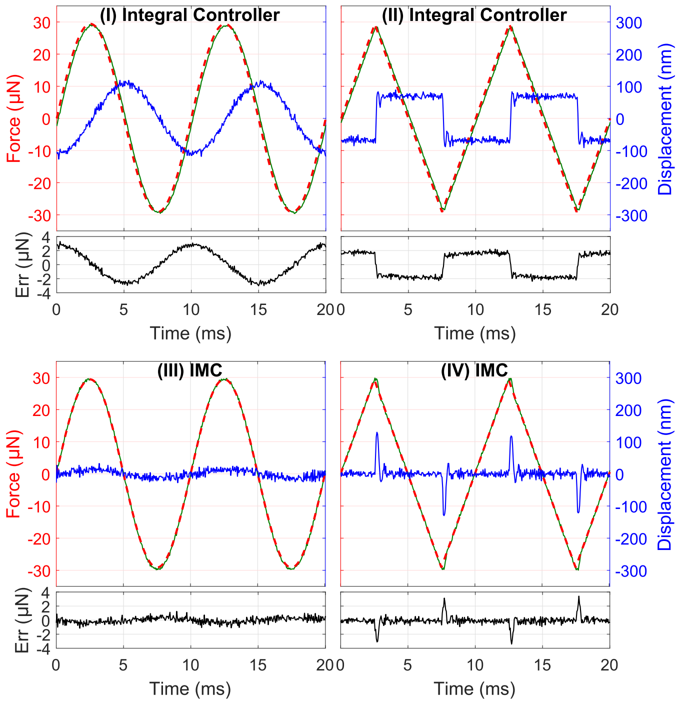

Fig. 13. Force sensing performance of the device using integral controller (I,II) and IMC (III,IV) obtained at $V_b = 0$V. The same behavior is observed for different V_b values. The left-hand scale is for external force (- -) and measured force (—) in micronewton, and the right-hand scale is the stage displacement (—) in nanometer. The error signal is obtained by subtracting the external and measured forces.

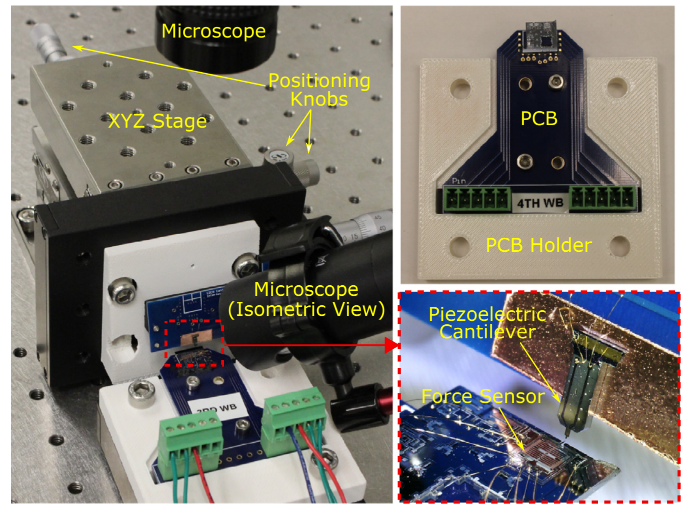

Fig. 14. The test setup for applying force to the force sensor using a microfabricated cantilever with a piezoelectric patch. The force sensor is glued and wire bonded on a PCB. The close-up shows the interaction between the force sensor and the cantilever.

Table 3
The 1σ-resolution of the force measurement at various stiffness-adjustment voltages in the open loop (O.L.) and closed loop (C.L.). The range of the force sensor in the open loop is also presented.

V_b	0 V	20 V	30 V	40 V	50 V	60 V
O.L. Res. (nN)	23.3	21.6	19.6	17.1	13.5	9.3
O.L. Range ($\pm$ μN)	42.6	39.6	36.2	31.6	25.3	15.4
IMC. Res. (nN)	19.1	17.9	16.4	14.8	13.0	12.9
Integ. Res. (nN)	27.3	24.1	22.2	19.5	16.6	13.0

and isometric views of the force sensor. The principle of operation of the setup is based on bringing the microfabricated piezoelectric cantilever into contact with the force sensor tip using the positioning stages and the microscopes. After the contact is established, piezoelectric cantilever is actuated to dynamically load the force sensor.

Characterization tests are also performed with another contact-mode AFM cantilever (App-Nano-SHOCON) which features no piezoelectric layer. This low-stiffness cantilever[2] is also immobilized on the PCB during the tests.

6.2. Open-loop characteristics

The full-scale range (FSR) of the force sensor in open loop can be determined by knowing its flexural stiffness and its maximum allowable displacement range. Based on the analytical model presented in Section 3.3, we expected that the minimum sensor displacement range, occurring at $V_b = 60$ V, to be $\pm 2\,\mu$m. However, as shown in Fig. 5, this range is reduced at $V_b = 60$ V, which is most likely due to the fabrication tolerances. Therefore, based on the experimental data, the linear displacement range of $\pm 2\,\mu$m is considered for the force sensor across all V_b up to 50 V, while the displacement range at $V_b = 60$ V is $\pm 1.75\,\mu$m. The force sensor's stiffness, on the other hand, is experimentally obtained in Section 4.2 for $V_b = 0$ V. The variation of the sensor resonant frequency with V_b, modeled in (19), is exploited in (31) to determine the stiffness of the sensor across all stiffness-adjustment voltages.

$$\frac{f_b}{f_0} = \sqrt{\frac{K_b}{K_0}} \tag{31}$$

Here, f_b and K_b respectively are the resonant frequency and stiffness at V_b, and f_0 and K_0 are the corresponding values at $V_b = 0$ V. Knowing the stiffness and the displacement range, the FSR of the force sensor is obtained at each V_b and presented in Table 3.

The bandwidth in open loop is defined as the frequency where the magnitude of the response shown in Fig. 6 varies by 3 dB with respect to its dc-level. The open-loop sensing bandwidth of the device changes from 2.35 kHz for $V_b = 0$ V to about 1.52 kHz for $V_b = 60$ V. Note that, the under-damped behavior of the device in open loop can also lead to oscillations and consequently a lower measurement bandwidth. This occurs when the input force contains high-frequency components near the resonant frequency of the force sensor. Triangular-shaped forces, for instance, should have a frequency about hundred times less than the resonance frequency to induce negligible oscillations on the force sensor [39].

Knowing the stiffness of the force sensor, the resolution of the displacement sensor (see Section 4.3) is converted to the force resolution and reported in Table 3. In order to obtain the force sensing resolution, noise data is filtered off-line according to the open-loop sensing bandwidth. The 1σ-resolution of 30.4 nN is obtained at $V_b = 0$ V, which is improved at higher values of V_b as the stiffness decreases.

The linearity of the force sensor in the open loop is also explored by employing the on-chip actuators. Using the data presented in Fig. 5, the displacement of probe as a function of actuation force is obtained for $V_b = 0$ V and depicted in Fig. 15. The conversion between the actuation voltage and force is performed using (17). Based on the Hook's law for linear flexures, the displacement and the force are proportional via the constant sensor stiffness (i.e. K_x in Table 2). Assuming a linear flexure, the probe displacement is also presented in Fig. 15. As is clear, the displacement of the probe, which is proportional to the output of the force sensor in the open loop, deviates from the linear for larger forces. The deviation remains within 10% in the input force range of

[2] The stiffness can vary from 0.01 N/m to 0.6 N/m as per the datasheet.

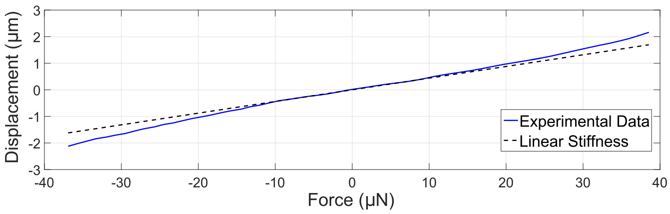

Fig. 15. The displacement of the probe as a function of actuation force. The dotted line shows the probe displacement assuming a linear stiffness of the flexures.

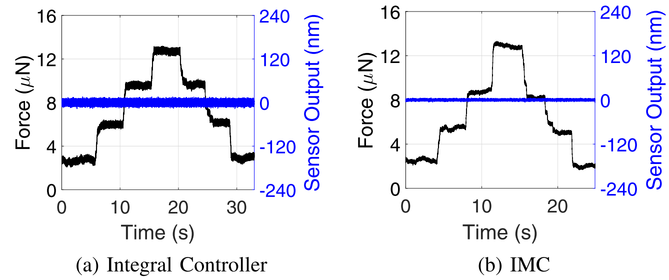

Fig. 16. A series of measurements performed to determine effectiveness of the two controllers in measuring the applied force. The stiffness-adjustment voltage was set to zero volt.

± 18 μ N and increases to about 28% in the full-scale range. Since the slight nonlinearity in the actuation force is already being accounted for in the conversion of actuation voltage to force, this nonlinearity is believed to be originated from the flexures. Even though this nonlinear behavior reduces for larger stiffness adjustment voltages, it negatively affects the accuracy of the force sensor. This can further justify the use of a feedback control system.

6.3. Open-loop test

We operated the force sensor in open loop to determine the stiffness of the piezoelectric cantilever. Using the test set up in Fig. 14, the force sensor is initially brought into contact with the cantilever while $V_b = 0$ V. Then, a triangular actuation signal (v_a) with the amplitude and offset of 5 V is applied to the electrostatic actuator of the force sensor to push and bend the cantilever. In the test, the cantilever and the force sensor remain in contact, and thus, they experience the same displacement. This displacement is measured using the piezoresistive sensor as a function of actuation voltage (v_a). Using (17), the actuation force is then calculated, and knowing the stiffness of the force sensor, the cantilever stiffness is easily determined as 33.5 N/m.

In the second test, we measured the force produced by the piezoelectric cantilever. The force sensor and the cantilever were brought into contact, and an actuation voltage of 10 V was applied to the cantilever's piezoelectric layer. The probe displacement was measured as 157 nm. Knowing the displacement and the stiffness of both force sensor and the cantilever, 8.573 μ N is obtained as the generated force. A conversion factor of 0.8573 μN/V is calculated between the produced force of the piezoelectric cantilever and its actuation voltage. This factor is used to perform further tests in closed loop.

6.4. Closed-loop characteristics

The closed-loop bandwidth of the force sensor was obtained as 3.6 kHz with an integral controller and 800 Hz with an IMC. To determine the sensor resolution, noise content of the control signal (u in Fig. 9) for both controllers was recorded. The measurements are performed with a sampling frequency of 25 kHz while a low-pass filter (Stanford Research SR 650) with a cutoff frequency of 10 kHz is placed in the path. The noise signal is then filtered off-line based on the bandwidth of the integral and internal model controllers and is converted to force using (17). The 1σ-resolution of the force sensor is presented in Table 3. Better than 28 nN resolutions are obtained for both controllers with the best value being 12.9 nN at $V_b = 60$ V for IMC.

The full-scale range (FSR) of the closed-loop force sensor depends only on the electrostatic actuator's characteristics. The FSR is obtained from (17) to be − 45.31 μN to 46.9 μ N, where a maximum actuation voltage of 85 V on the comb drive is allowed. This voltage is selected to avoid snap-in instability [14].

6.5. Closed-loop test

Force measurement test in closed-loop is initially performed using the compliant cantilever App-Nano-SHOCON. First, the cantilever tip and the force sensor are brought into contact. Then, using the positioner shown in Fig. 14, the displacements of 10 μ m, 20 μ m and 30 μ m are applied to the base of the cantilever, and afterwards, the cantilever positioner is moved back following similar displacement steps. The controller signal is then converted to force using (17). As is clear from Fig. 16, both controllers preform well in maintaining the null position of the force sensor. Cantilever stiffness is found to be approximately 0.3 N/m which is within the range stated in the manufacturer data sheet.

The piezoelectric cantilever characterized in Section 6.1 is used in the second experiment. Unlike the App-Nano-SHOCON, the piezoelectric cantilever has a stiffness comparable to that of the force sensor. Note that the feedback controllers are designed based on the assumption that a pure external force is applied to the force sensor. In this test, however, due to the comparable stiffness of the piezoelectric cantilever, the force sensor dynamics are altered. To investigate this issue, the initial contact is established between the sensor and the cantilever, and then the frequency response of the coupled system from the force sensor electrostatic actuator to its piezoresistive displacement sensor output is obtained. The response is compared with force sensor's primary response (with no contact) in Fig. 17, while the stiffness-adjustment voltage is set to 0 V. A significant deviation is noticeable between the response of the coupled system and the force sensor. The increasing resonance frequency and decreasing dc-gain are signs that the system is stiffening due to the mechanical contact. Therefore, in order to use the closed-loop force sensor, the controller should be retuned accordingly. This can be easily performed in our controller through a gain adjustment.

Having retuned the controller gain, the closed-loop force sensor is brought into contact with the cantilever. An initial force is established to ensure that the sensor and the cantilever remain in contact throughout the experiments. A step signal is applied to the piezoelectric actuator of the cantilever, and response of the force sensor with the integral controller and IMC are recorded and plotted in the Fig. 18 with $V_b = 0$ V. The force sensor output perfectly tracks the input exogenous force. The voltage applied to the piezoelectric cantilever is converted to the input external force using the conversion factor of 0.925 μN/V. This is about 8% larger than 0.8573 μN/V obtained in the open-loop test. The difference can be attributed to the test condition variations as the contact point of the force sensor and cantilever can be different along the cantilever length. Similar results are observed for other stiffness-adjustment voltages. Compared to the integral controller, the rise time and the probe displacement are smaller under the IMC. However, this controller response contains ringing and overshoot.

In another experiment, the piezoelectric cantilever is driven with a 5 Hz sinusoidal and triangular signals with the stiffness adjustment voltages being adjusted to 0 V. As shown in Fig. 19, the implemented controllers work to keep the probe at zero position. Using the integral controller, however, the force sensor response to triangular external force shows a small offset as depicted in Fig. 19a (II) which is eliminated by IMC in Fig. 19b (II).

The highest RMS of the tracking error is about 102 nN occurred for the integral controller with the sinusoidal input. With the IMC, a

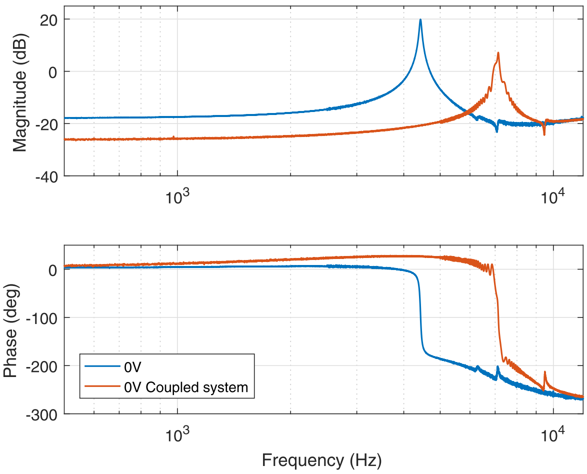

Fig. 17. Coupled system frequency response from the force sensor actuation to its piezoresistive sensor output compared with the response of the force sensor at $V_b = 0$ V.

tracking error of 82 nN is obtained for both triangular and sinusoidal inputs. Here, since the error appears to be completely stochastic, a RMS value close to the resolution, reported for closed-loop in Table 3, was expected. The larger RMS error is probably due to the re-tuning of the controllers' gains. In addition, the closed-loop noise is recorded in an isolation box, whereas, the stiffness test is performed under normal laboratory conditions.

7. Discussion

To further explore the force sensor performance, we may define the dynamic range (DNR) of the sensor (in *dB*) as [40]:

$$DNR = 20 \times log\left(\frac{FSR}{Resolution}\right). \tag{32}$$

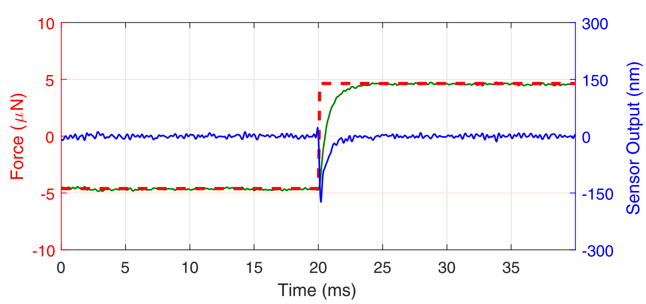

(a) Integral Controller

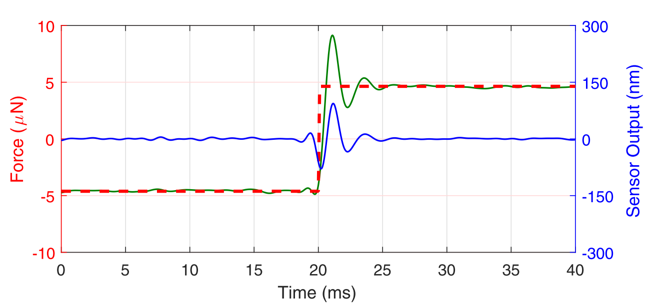

(b) IMC

Fig. 18. Step response of (a) the integral controller and (b) IMC at $V_b = 0$ V. The sensor output (—), the input external force (- -), and the force sensor output (—) are presented.

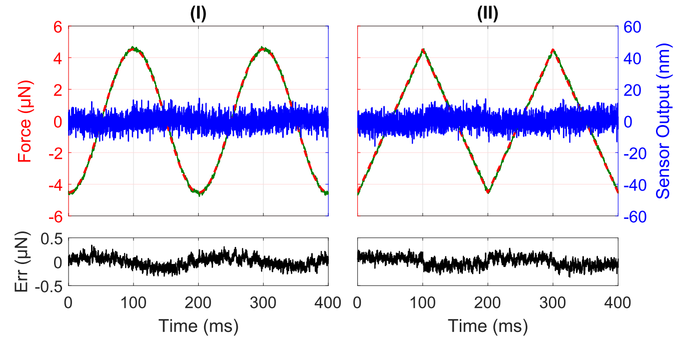

(a) Integral controller

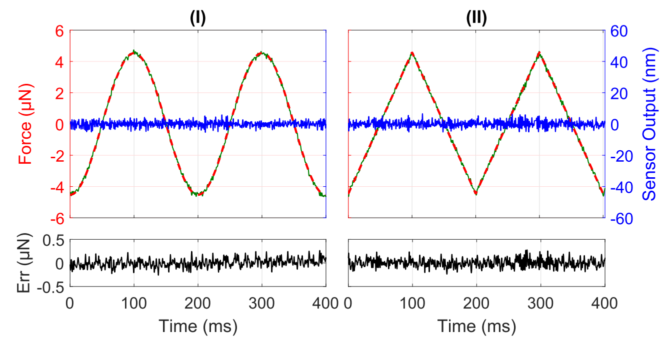

(b) IMC

Fig. 19. Cantilever force measurement using integral controller (a) and IMC (b) obtained at stiffness-adjustment voltages of 0V. The left-hand axis is for external force (- -) and measured force (—) in micronewton, and the right-hand axis is for stage displacement (—) in nanometer.

In open loop, the 1σ-resolution of 30.4 nN and FSR of $\pm$ 42.6 μ N are obtained for the force sensor with $V_b = 0$ V, which gives a DNR of 65 dB. Since both FSR and the sensing resolution in open loop are proportional to the sensor stiffness, the force sensor DNR is obtained to be fairly constant at 65 dB for all values of V_b. However, due to a smaller achievable displacement range at $V_b = 60$ V, the DNR slightly decreases to 64.3 dB.

The FSR in closed loop depends on the actuator properties and thus remains constant across all values of V_b. Hence, the sensor dynamic range can be modified here by manipulating the resolution using the stiffness-adjusting voltage. Using the resolution values reported in Table 3 for the integral controller, the sensor DNRs can be calculated. The DNR increases from 64.7 dB at $V_b = 0$ V to about 71.1 dB for $V_b = 60$ V. The same trend is observed for the force sensor with IMC, i.e. the DNR is obtained to be 67.8 dB and 71.2 dB for $V_b = 0$ V and $V_b = 60$ V, respectively. Note that in both open and closed loop, we have only considered the positive side of the full-scale range to calculate DNR. If we consider the push-pull measurement capability of the force sensor, the FSR can be roughly doubled and the dynamic range increased by about 6 dB.

In Table 4, performances of a number of previously reported force sensors are compared with the present work. The DNR obtained in this work is comparable with previously reported sensors, proving that the proposed closed-loop force sensor can offer a similar performance. However, this force sensor comes with a number of added advantages. The closed-loop configuration of the sensor removes the adverse affect of the flexural nonlinearities at the output, while by adding more comb-drive actuators the full-scale range and DNR can be easily increased. Note that having a larger FSR in typical open-loop MEMS force sensors (such as those in Table 4) can be directly translated to a larger displacement requirement for the micro-sized flexures which adds more complexity to their design and/or more measurement nonlinearity.

Table 4
Comparing the performance of this MEMS force sensor with previously reported sensors. The designs are categorized based on whether the sensor functions in the open loop (O.L.) and closed loop (C.L.)

Ref.	This work	[41]	[3]	[9]	[21]	[17]
FSR(μN)	− 45.3 to 46.9	360	48	110	7.6	1
Res.(nN)	12.9	70	37.9	33.2	1.39	0.05
DNR (dB)	71.2	74.2	62.1	70.4	70.8	86.0
Design	C.L.	O.L.	C.L.	O.L.	O.L.	O.L.

In addition, the constant stiffness of previously-proposed force sensors in Table 4 limits the range of samples that can be used in force measurement. By proposing and implementing the stiffness-adjustment mechanism in this work, the device stiffness can be manipulated rendering it conducive to force measurement for a variety of samples with lower stiffnesses. In addition by using this mechanism, the resolution, and therefore, the dynamic range of the closed loop sensor can be easily manipulated as needed. In this work, this tuning “knob” enabled us to enhance the resolution of the sensor in closed loop approximately 1.5 times to reach 12.9 nN.

Another advantage of the proposed closed-loop force sensor is its sensing bandwidth. While the sensors in Table 4 are designed for static and low-frequency force measurements, we have demonstrated a sensing bandwidth of 800 Hz and 3.6 kHz for the IMC, and the integral controller, respectively.

A drawback of using the closed-loop system, however, is the potential occurrence of instabilities if the force sensor interacts with samples of a comparable and/or larger stiffness. Here, we were able to address this issue by adjusting controller gains. Future attempts will involve the design of controllers that offer better robustness.

8. Conclusion

Considering the shortcomings of the existing technology in force sensing with MEMS, this paper presented a novel 1-DoF MEMS force sensor, featuring on chip actuation, sensing, and stiffness-adjusting mechanisms. The proposed design renders the MEMS force sensor conducive to feedback control as well as *in-situ* tuning of its mechanical stiffness. The proposed analytical models for the stiffness-adjusting and actuation mechanisms are employed for the design of the MEMS force sensor and later on for its calibration using experimental data. During the calibration, three tests were performed to determine unknown sensor parameters.

The characterization reveals that the device features a resonant frequency of 4.48 kHz which can be reduced to 2.88 kHz by employing the embedded stiffness-adjusting mechanism. This translates to about 2.4 times decrease in the device's stiffness making it more suitable for force sensing of soft samples. A resolution of 1.43 nm was obtained for the on-chip displacement sensor, and by proposing a test setup, the sensing properties of the MEMS device were investigated. In open loop, a sensing resolution of 23.3 nN within a bandwidth of 2.35 kHz and a full-scale range of $\pm$ 42.6 μN are experimentally obtained. The resolution can also be enhanced to 9.3 nN by employing the active compliance mechanism, at the price of reducing the full-scale range to $\pm$ 15.4 μN. The flexural nonlinearity in the open loop was found to be less than 10 % within the range of $\pm$ 18 μN. The adverse effect of the flexural nonlinearity is avoided by implementing feedback controllers. Integral and IMC controllers were separately implemented. Both controllers are added to a resonant control loop that serves as a damping controller. In closed loop, the full-scale range is only a function of the actuation and was found to be − 45.31 μN to 46.9 μN. With the integral controller, the finest resolution of 13 nN is achieved at $V_b = 60$ V within a bandwidth 3.6 kHz. The phase lag problem observed with the integral controller is addressed by implementing an IMC controller, through which a bandwidth of 800 Hz is achieved with a resolution of 12.9 nN at $V_b = 60$ V. While the closed-loop MEMS force sensor operates as expected for soft samples such as a compliant AFM cantilever, the performance of the controllers and their stability are degraded throughout the sensor interaction with a stiff cantilever. Design of more robust controllers is left as future work. Although the performance of the proposed force sensor are comparable with the previously-reported sensors, the added advantages of closed-loop operation and the stiffness-adjusting mechanism make this device a better candidate for use in high-precision and high-bandwidth force measurement applications.

Acknowledgment

This research was supported by UT-Dallas and a UT-STARS grant.

References

[1] Han T, Williams JM, Beebe TP. Chemical bonds studied with functionalized atomic force microscopy tips. Analytica Chimica Acta 1995;307(2):365–76.
[2] Oberhauser AF, Marszalek PE, Erickson HP, Fernandez JM. The molecular elasticity of the extracellular matrix protein tenascin. Nature 1998;393(May (6681)):181–5.
[3] Moore SI, Coskun MB, Alan T, Neild A, Moheimani SOR. Feedback-controlled MEMS force sensor for characterization of microcantilevers. J Microelectromech Syst 2015;24(August (4)):1092–101.
[4] Coskun MB, Moore S, Moheimani SR, Neild A, Alan T. Zero displacement microelectromechanical force sensor using feedback control. Appl Phys Lett 2014;104(15):153502.
[5] Piriyanont B, Fowler AG, Moheimani SOR. Force-controlled MEMS rotary microgripper. J Microelectromech Syst 2015;24(August (4)):1164–72.
[6] Qu J, Zhang W, Jung A, Cruz SSD, Liu X. Microscale compression and shear testing of soft materials using an MEMS microgripper with two-axis actuators and force sensors. IEEE Trans Autom Sci Eng 2017;14(April (2)):834–43.
[7] Yang S, Xu Q, Nan Z. Design and development of a dual-axis force sensing MEMS microgripper. J Mech Robot 2017;9(October (6)):061 011–061 011–9.
[8] Lopez D, Decca RS, Fischbach E, Krause DE. MEMS-based force sensor: Design and applications. Bell Labs Tech J 2005;10(3):61–80.
[9] Kim K, Cheng J, Liu Q, Wu XY, Sun Y. Investigation of mechanical properties of soft hydrogel microcapsules in relation to protein delivery using a MEMS force sensor. J Biomed Mater Res Part A 2010;92A(1):103–13.
[10] Kohyama S, Takahashi H, Yoshida S, Onoe H, Shoji KH, Tsukagoshi T, Takahata T, Shimoyama I. MEMS force and displacement sensor for measuring spring constant of hydrogel microparticles. 2017 IEEE 30th International Conference on Micro Electro Mechanical Systems (MEMS), 22-26 Jan.. 2017. p. 1040–3.
[11] Park H, Thanh-Vinh N, Hirayama K, Tsukagoshi T, Noda K, Takahata T, Matsumoto K, Shimoyama I. Measuring the vibration of cells subjected to ultrasound using a MEMS-based force sensor array. 2016 IEEE 29th International Conference on Micro Electro Mechanical Systems (MEMS), 24-28 Jan.. 2016. p. 695–7.
[12] Lin G, Pister KSJ, Roos KP. Surface micromachined polysilicon heart cell force transducer. J Microelectromech Syst 2000;9(March (1)):9–17.
[13] Sun Y, Wan KT, Roberts KP, Bischof JC, Nelson BJ. Mechanical property characterization of mouse zona pellucida. IEEE Trans NanoBiosci 2003;2(December (4)):279–86.
[14] Maroufi M, Fowler AG, Moheimani SOR. MEMS for nanopositioning: Design and applications. J Microelectromech Syst 2017(99):1–32.
[15] Awtar S, Slocum AH, Sevincer E. Characteristics of beam-based flexure modules. J Mech Des 2006;129(May (6)):625–39.
[16] Frisch-Fay R. Flexible Bars. Butterworths: ser. Butterworths scientific publications; 1962.
[17] Rajagopalan J, Tofangchi A, Saif MTA. Linear high-resolution biomems force sensors with large measurement range. J Microelectromech Syst 2010;19(December (6)):1380–9.
[18] Nastro A, Ferrari M, Russo AL, Ardito R, Ferrari V. Servo-assisted position-feedback mems force sensor with tunable sensitivity and sub-nanonewton range. 2017.
[19] de Laat MLC, Garza HHP, Herder JL, Ghatkesar MK. A review on in situ stiffness adjustment methods in MEMS. J Micromech Microeng 2016;26(6):063001.
[20] Walter B, Faucher M, Algre E, Legrand B, Boisgard R, Aime JP, Buchaillot L. Design and operation of a silicon ring resonator for force sensing applications above 1 MHz. J Micromech Microeng 2009;19(11):115009.
[21] Zhao C, Wood GS, Xie J, Chang H, Pu SH, Kraft M. A force sensor based on three weakly coupled resonators with ultrahigh sensitivity. Sens Actuators A 2015;232.
[22] Maroufi M, Bazaei A, Mohammadi A, Moheimani SOR. Tilted beam piezoresistive displacement sensor: Design, modeling, and characterization. J Microelectromech Syst 2015;24(5):1594–605.
[23] Maroufi M, Fowler AG, Moheimani SOR. MEMS nanopositioner for on-chip atomic force microscopy: A serial kinematic design. J Microelectromech Syst 2015;24(December (6)):1730–40.
[24] Krijnen B, Hogervorst RP, van Dijk JW, Engelen JBC, Woldering LA, Brouwer DM, Abelmann L, Soemers HMJR. A single-mask thermal displacement sensor in MEMS. J Micromech Microeng 2011;21(7).
[25] Guliyev E, Volland BE, Sarov Y, Ivanov T, Klukowski M, Manske E, Rangelow WI. Quasi-monolithic integration of silicon-MEMS with piezoelectric actuators for high-speed non-contact atomic force microscopy. Meas Sci Technol 2012;23(7):8.

[26] Maroufi M, Fowler AG, Moheimani SOR. MEMS for nanopositioning: Design and applications. IEEE J Microelectromech Syst 2017;26(3):469–500.
[27] Maroufi M, Moheimani SOR. A 2DOF SOI-MEMS nanopositioner with tilted flexure bulk piezoresistive displacement sensors. IEEE Sens J 2016;16(April1(7)):1908–17.
[28] Maroufi M, Moheimani SOR. Characterization of piezoresistive and electrothermal sensors in MEMS devices. IEEE Sensors Conference. FL., USA: Orlando; 2016.
[29] Cowen A, Hames G, Glukh K, Hardy B. PiezoMUMPs Design Handbook. 2014.
[30] Grade JD, Jerman H, Kenny TW. Design of large deflection electrostatic actuators. J Microelectromech Syst 2003;12(June (3)):335–43.
[31] Fowler AG, Maroufi M, Bazaei A, Moheimani SOR. MEMS nanopositioner for lissajous-scan atomic force microscopy. ASME Dynamic Systems and Control Conference,October 22-24, San Antonio, TX, USA 2014. Texas, USA: San Antonio; 2014.
[32] Fanson JL, Caughey TK. Positive position feedback control for large space structures. AIAA J 1990;28(4):717–24.
[33] Bhikkaji B, Ratnam M, Moheimani S. PVPF control of piezoelectric tube scanners. Sens Actuators A 2007;135(2):700–12.
[34] Aphale SS, Fleming AJ, Moheimani SOR. Integral resonant control of collocated smart structures. Smart Mater Struct 2007;16(2):439.
[35] Pota HR, Moheimani SOR, Smith M. Resonant controllers for smart structures. Smart Mater Struct 2002;11(1):1.
[36] Maroufi M, Alemansour H, Moheimani SOR. A closed-loop MEMS force sensor with adjustable stiffness. 2017 IEEE Conference on Control Technology and Applications (CCTA), 27-30 Aug.. 2017. p. 438–43.
[37] Goodwin G, Graebe S, Salgado M. Control System Design. Prentice Hall; 2001.
[38] Bazaei A, Maroufi M, Fowler AG, Moheimani SOR. Internal model control for spiral trajectory tracking with mems afm scanners. IEEE Trans Control Syst Technol 2016;24(September (5)):1717–28.
[39] Devasia S, Eleftheriou E, Moheimani SOR. A survey of control issues in nanopositioning. IEEE Trans Control Syst Technol 2007;15(5):802–23.
[40] Fleming AJ. A review of nanometer resolution position sensors: Operation and performance. Sens Actuators A 2013;190:106–26.
[41] Beyeler F, Neild A, Oberti S, Bell DJ, Sun Y, Dual J, Nelson BJ. Monolithically fabricated microgripper with integrated force sensor for manipulating microobjects and biological cells aligned in an ultrasonic field. J Microelectromech Syst 2007;16(February (1)):7–15.

Mohammad Maroufi graduated with double B.Sc. degrees in Mechanical Engineering and Applied Physics as a distinguished student from Amirkabir University of Technology (Tehran Polytechnic) in 2008. He obtained his master's degree in Mechatronics at the same university in 2011, and he received his Ph.D. in Electrical Engineering at the University of Newcastle, Australia in 2015.

Mohammad Maroufi is currently a Research Associate with the Department of Mechanical Engineering, University of Texas at Dallas, Richardson, TX, USA. His research interests include development of high-precision mechatronic systems, design and control of MEMS nanopositioners, microsensors design, and video-rate Atomic Force Microscopy.

Hamed Alemansour received the B.Sc. and M.Sc. degrees in mechanical engineering from the Shiraz University and the Sharif University of Technology, in 2011 and 2013, respectively. He is currently pursuing the PhD degree in mechanical engineering with the University of Texas at Dallas, Richardson, TX, USA. His current research interests include the characterization and control of MEMS-based devices, AFM microcantilevers and scanning tunneling microscopes.

M. Bulut Coskun received the B.Sc. and M.Sc. degrees in mechatronics engineering from Sabanci University, Istanbul, Turkey, in 2009 and 2011, respectively, and the Ph.D. degree in mechanical and aerospace engineering from Monash University, Australia, in 2015. Later on, he joined the Department of Mechanical Engineering, University of Texas at Dallas, as a Research Associate. His current research interests include the design, analysis, fabrication, and characterization of microelectromechanical systems with a particular emphasis on novel microsensors, developing active microcantilevers for high-speed atomic force microscopy applications, and graphene-based sensors.

S.O. Reza Moheimani currently holds the James Von Ehr Distinguished Chair in Science and Technology in Department of Mechanical Engineering at the University of Texas at Dallas. He is also an Adjunct Professor at the University of Newcastle, Australia. His current research interests include ultrahigh-precision mechatronic systems, with particular emphasis on dynamics and control at the nanometer scale, including applications of control and estimation in nanopositioning systems for high-speed scanning probe microscopy and nanomanufacturing, modeling and control of microcantilever-based devices, control of microactuators in microelectromechanical systems, and design, modeling and control of micromachined nanopositioners for on-chip scanning probe microscopy and atomically precise lithography.

Dr. Moheimani is a Fellow of IEEE, IFAC and the Institute of Physics, U.K. His research has been recognized with a number of awards, including IFAC Nathaniel B. Nichols Medal (2014), IFAC Mechatronic Systems Award (2013), IEEE Control Systems Technology Award (2009), IEEE Transactions on Control Systems Technology Outstanding Paper Award (2007) and several best paper awards in various conferences. He is Editor-in-Chief of Mechatronics and has served on the editorial boards of a number of other journals, including IEEE Transactions on Mechatronics, IEEE Transactions on Control Systems Technology, and Control Engineering Practice. He chaired the IFAC Technical Committee on Mechatronic Systems 2011–2017.